Design Optimization of a Switched Reluctance Machine with an Improved Segmental Rotor for Electric Vehicle Applications

Yuanfeng Lan [1,2], **Mohamed Amine Frikha** [1,2], **Julien Croonen** [1,2], **Yassine Benômar** [1,2], **Mohamed El Baghdadi** [1,2] **and Omar Hegazy** [1,2,*]

1   MOBI-EPOWERS Research Group, ETEC Department, Vrije Universiteit Brussel (VUB), Pleinlaan 2, 1050 Brussels, Belgium
2   Flanders Make, Gaston Geenslaan 8, 3001 Heverlee, Belgium
*   Correspondence: omar.hegazy@vub.be; Tel.: +32-2-629-2992

Abstract: In this article, a switched reluctance machine (SRM) with six phases and a misaligned segmental rotor is proposed. The segmental rotor has an internal 15-degree misalignment, allowing the SRM structure to be a one-layer 2D structure with a short flux path structure. The proposed SRM produces a relatively low torque ripple by exciting two phases simultaneously. Additionally, an optimization method is applied, allowing for the maximum torque position of one phase to be aligned with the zero-torque position of the adjacent phase. The finite element method (FEM) is used to analyze and design the proposed SRM and to simulate the proposed liquid cooling system. The static torque waveforms are analyzed, and the dynamic torque waveforms are simulated with a drive using SiC MOSFETs. Finally, a prototype is manufactured, and the experiment is performed to validate the design and simulation results.

Keywords: switched reluctance machine; segmental rotor; torque ripple; finite element method; multi-stack; electric vehicles

1. Introduction

The switched reluctance machine (SRM) has received increasing attention as a potential electric machine for electric vehicle (EV) applications. It has advantages, such as structure simplicity, high robustness, high reliability and low manufacturing costs [1,2]. The main disadvantages of the SRM are the torque ripple and limited torque density. Numerous research studies were conducted to introduce different approaches to reduce the torque ripple or increase the average torque. The SRM with a segmental rotor is one of these approaches. The study presented in [3] demonstrated an SRM with a segmental rotor. This SRM obtained significant performance improvement compared to the conventional one. Furthermore, in [4], an 80 kW SRM with a segmental rotor was developed. The optimization results showed that this SRM is likely to be able to produce an equivalent performance as a class-leading Internal Permanent Magnet (IPM) machine. Moreover, in [5], an SRM with a segmental rotor was proposed. From the simulation results, the average torque increased by 6.5%, and the torque ripple reduced by 2.0% compared to the reference SRM.

The multi-layer structure is another approach to reducing the torque ripple as shown in [6], where a two-layer SRM was proposed. A multi-layer SRM was proposed by [7] to reach a lower torque ripple. A double layer per phase SRM was presented by [8], and a prototype was built and tested. In [9], an SRM with a multilayer structure was proposed. The simulation results show that it is a promising SRM structure. The study [10] analyzed a multi-layer SRM with a magnetic equivalent circuit (MEC) model. A novel shape design method was introduced to decrease the torque ripple of a multi-layer SRM. A combination of a multi-layer and segmental rotor was introduced by [11]. It was a two-step multi-layer rotor from the segmental type. The SRM with a segmental and multi-layer rotor increased

the average torque by 10% and reduced the torque ripple by 19% compared to an SRM with a segmental rotor but without a multi-layer rotor.

The asymmetric rotor or stator is an important approach to design an SRM with reduced torque ripple. The article [12] introduced a three-phase 12/10 asymmetric SRM. Finite element method (FEM) simulation was used to analyze the SRM. The study [13] presented a 6/4 asymmetric stator SRM. The air-gap length and the width of stator poles were analyzed. A two-phase SRM with an asymmetric rotor was proposed in [14]. The asymmetric rotor provides the SRM the capability to start from various initial rotor positions. The research [15] proposed a control method for an asymmetric rotor SRM, by focusing on its torque ripple performance. An asymmetric rotor SRM was presented in [16] to reduce the torque ripple. The design method was introduced in the cited study. Compared to a conventional SRM, the presented SRM reduced the torque ripple by 10%. An asymmetric rotor bearingless SRM was introduced in [17] to reduce the torque ripple. The introduced SRM has 20% lower torque ripple compared to a conventional bearingless SRM. In general, the steps on the asymmetric rotor or stator poles increased the total reluctance between the rotor and stator poles when the rotor pole is at the aligned position. The proposed SRM in this paper does not have the step structure and has identical air-gap length when the rotor pole is at the aligned position. It is an advantage to decrease the reluctance and increase the output torque, compared to the asymmetric rotor or stator structure.

The cooling system is an important aspect of SRM design as well. The research [18] introduced a 10 kW liquid cooled SRM and its thermal model. The model was used to optimize the cooling system. A liquid-cooled SRM with a coolant jacket structure was proposed in [19]. A dual-flute helical heat exchanger was used for the cooling jacket. The study [20] proposed a thermal model for an SRM for high-speed applications. An evaporative cooling SRM and a conventional SRM were compared in [21]. The results show that the evaporative cooling method decreases the magnitude of the radial electromagnetic force. An improved thermal lumped parameter model was proposed and validated in [22] for SRMs. An advanced direct coil cooling method for SRMs is modelled and tested in [23]. Compared to a standard water jacket cooling method, the cooling method proposed in [23] indicates a 47.8% power density improvement and 52.8% thermal performance gain.

This article proposes an improved SRM with a misaligned segmental rotor. The rated power of the proposed SRM is 2 kW, which represents a reduced scaled prototype for experimental tests for an 80 kW full scale SRM for EV applications. The rated speed of the proposed SRM is 3000 rpm; the rated torque is 6.5 Nm. It is a combination of a multi-layer SRM and a segmental rotor SRM. Notably, the multi-layer structure is designed for a 2D structure by misaligning the rotor segments with a short flux path configuration. It simplifies the SRM structure to make it easier to analyze and manufacture. With the adopted method where two machine phases are excited simultaneously, the power density of the proposed SRM is increased. With the FEM optimization method, the pole shape of the proposed SRM is designed to achieve lower torque ripple. The structure and method of operation of the proposed SRM are introduced in Section 2. In Section 3, the electromagnetic analysis is conducted with finite element analysis (FEA), and an optimization method is presented. In Section 4, the liquid cooling system is analyzed and tested. In Section 5, the SiC driver and dynamic simulation of the proposed SRM system are analyzed. The prototype of the proposed SRM and the experimental results are presented in Section 6, and conclusions are drawn in Section 7.

2. Structure and Operation Method of the Proposed SRM

This section presents the basic structure and the operation method of the proposed SRM. Figure 1a shows the structure of the proposed SRM, which is a six-phase SRM with a misaligned rotor segment. Two of the rotor segments are misaligned by 15 degrees. With the misaligned rotor segments, the proposed SRM has two phases working simultaneously. It means one out of three phases is working when it is running. The conventional SRM in Figure 1b is the reference SRM, compared to the proposed SRM.
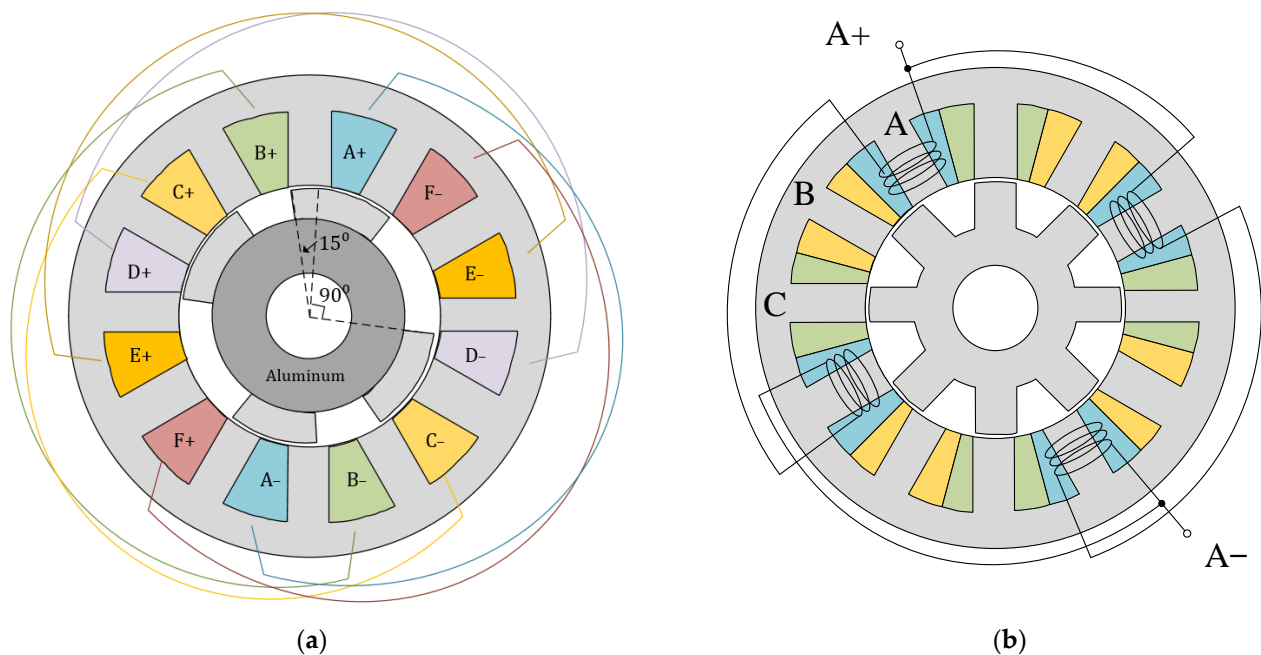
Figure 1. The structure of the SRMs: (**a**) the proposed segmental SRM; (**b**) a conventional SRM.

The conventional SRM is a three-phase SRM. Typically, it has one out of three phases working simultaneously. The operational phase number ratio of the conventional SRM is the same for the proposed SRM. As a result, the conventional three-phase SRM is selected to be the reference SRM.

The parameters of the SRMs are listed in Table 1. The proposed SRM and the conventional SRM have the same volume and air-gap length. They also have the same number of turns and the same number of stator poles.

Table 1. Parameters of the proposed SRM and the conventional SRM.

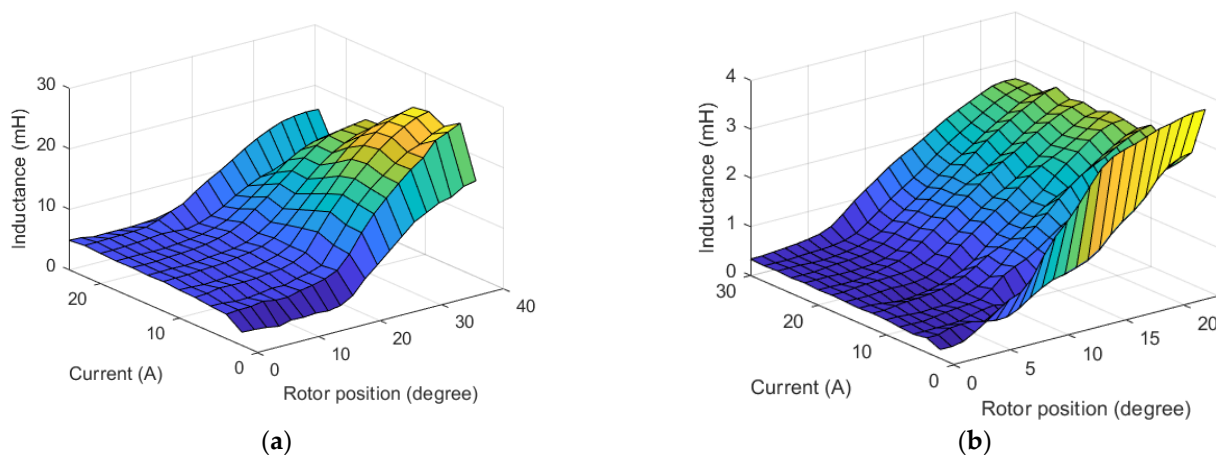| Parameter	Proposed SRM	Conventional SRM
Stator outer diameter (mm)	139.6	139.6
Lamination thickness (mm)	0.35	0.35
Stator pole height (mm)	23.27	19.3
Stator inner diameter (mm)	71.62	84
Rotor outer diameter (mm)	71.12	83.5
Rotor pole height (mm)	10.72	14.75
Air-gap length (mm)	0.25	0.25
Stack length (mm)	120	120
Number of phases	6	3
Number of phases working simultaneously	2	1
Copper winding length per phase (m)	37.12	32
Number of turns per phase	64	64
Number of stator poles	12	12
Number of rotor poles	4	8
Number of rotor pole pairs	1	4
Maximum average static torque (Nm)	23.9	6.6

From the Table 1, it can be seen that the copper-winding length per phase of the proposed SRM is 16% longer than the conventional SRM. Furthermore, the proposed SRM has six phases, and the conventional SRM has three phases. It means that the proposed SRM contains considerably more copper than the conventional SRM. Due to this reason, the total efficiency of the proposed SRM is lower than the conventional SRM. This is the main disadvantage of the proposed SRM. On the other hand, the torque output performance of

the proposed SRM has increased considerably due to the copper increase. With the same maximum current 35 A, the average static torque of the proposed SRM is 23.9 Nm. It is 6.6 Nm for the conventional SRM. Figure 2 presents the windings of the two SRMs.

(a)   (b)
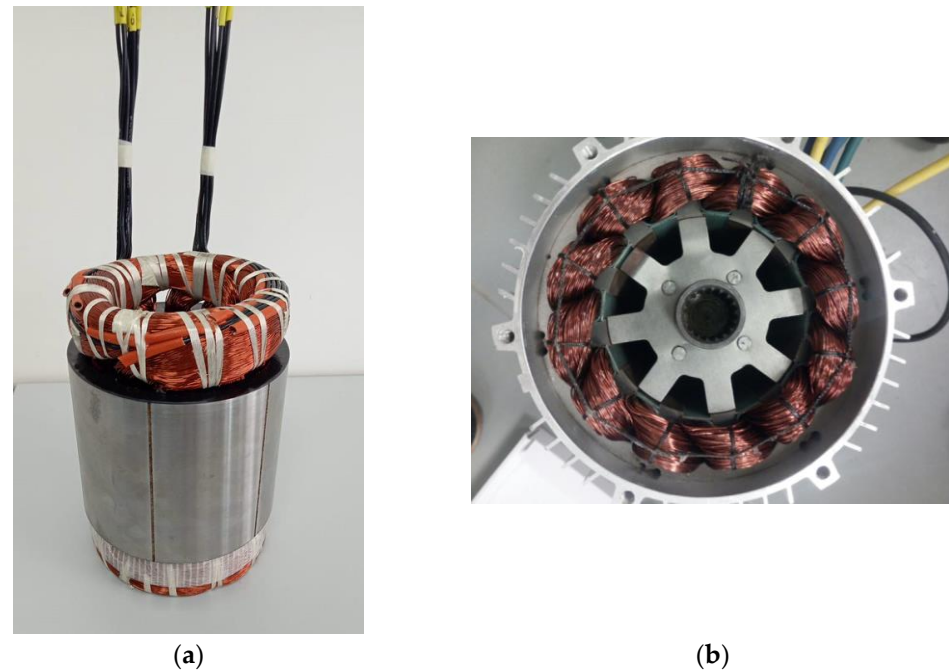
**Figure 2.** Windings of SRMs: (**a**) the proposed segmental SRM; (**b**) the conventional SRM.

Figure 3 demonstrates the inductance of winding for the SRMs from the unaligned to the aligned position. The proposed SRM has higher winding inductance compared to the conventional SRM. The reason is the difference of the winding lengths of the two SRMs.

(a)   (b)

Figure 3. Measured winding inductance of SRMs: (**a**) the proposed segmental SRM; (**b**) the conventional SRM.

Figure 4b presents the working method of the conventional three phases SRM [24,25]. Figure 4a shows the working method of the proposed SRM and illustrates the method to reduce the torque ripple. Where the T_A, T_B, T_C, T_D, T_E, T_F and T_{total} means the positive torque of phase A, B, C, D, E, F and the total positive torque, respectively. With the 15-degree misalignment and two phases working simultaneously, the torque of each phase can be summed to produce the total output torque and reduce the torque ripple. Furthermore, as there are two phases working together, the power density of the proposed SRM can be doubled compared to the conventional six-phase SRM.

It can be seen from Figure 4b that when the SRM is in commutation from one phase to a different phase, both involved phases produce a low torque. It results in the low sum torque during the commutation process. Figure 4a shows that two phases are working simultaneously for the proposed SRM. When one phase is in commutation, there is always another phase producing high torque. This method of operation reduces the torque ripple.
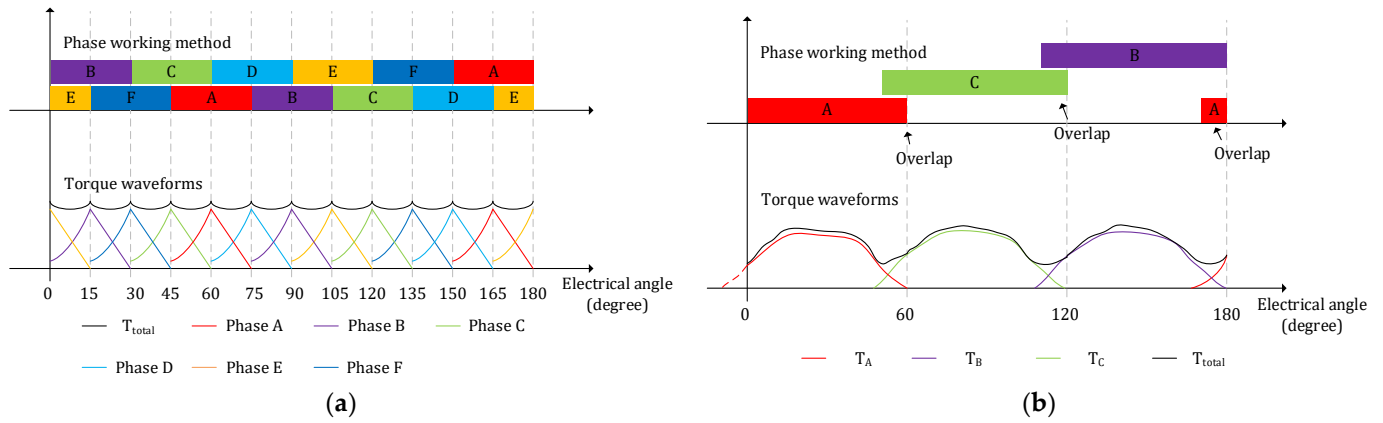

Figure 4. The operation method of the SRMs: (**a**) proposed six-phase SRM; (**b**) conventional three-phase SRM.

The torque curve of each phase is designed by FEM with optimization methods and shifted 30 degrees as the stator poles pitch satisfies the equation:

$$\alpha = 360° / \text{Ns} = 360° / 12 = 30° \tag{1}$$

where α is the stator pole pitch, and Ns is the number of stator poles.

Figure 5 presents the flux lines of the proposed SRM for phase A. In Figure 5a, phase A is energized, when the previous phase, phase F, is aligned. During operation, the excitation of phase A should start at this position. Figure 5b shows the flux lines when the segment is aligned with phase A. During operation, the demagnetization of phase A should finish at this point.
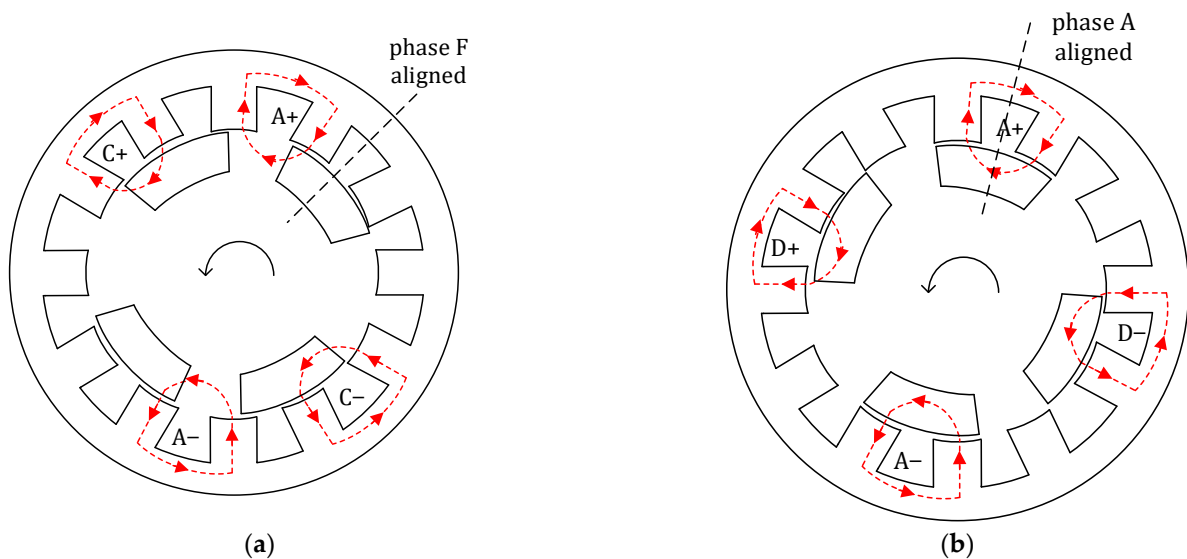
Figure 5. Magnetic fields of the proposed SRM: (**a**) magnetic fields when the previous phase of phase A is aligned; (**b**) magnetic fields when phase A is aligned.

Figure 6 shows the CAD model of the proposed SRM. This CAD model is used for FEM analysis and prototype manufacture.
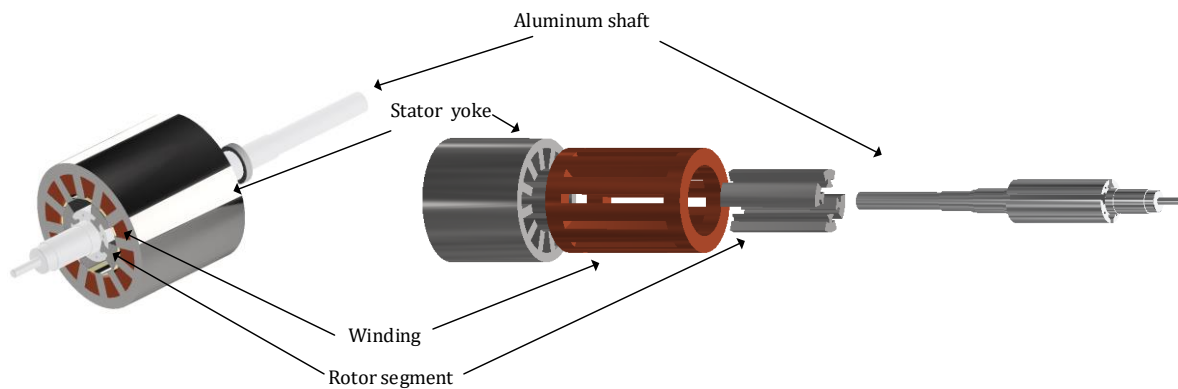
Figure 6. CAD model of the stator and rotor of the proposed SRM.

3. Electromagnetic Analysis and Optimization Method of the SRM

With the 2D FEM technique, the proposed SRM is analyzed and designed. Figure 7 displays the FEM simulation results of the proposed SRM.

The stator and rotor pole shapes are designed with the optimization method, for which the results are shown in Figure 8. It is illustrated in Figure 4 that the distance between the peak torque position and the aligned zero torque position should be 15 degrees which means the maximum torque should appear at a 75-degree point. Figure 8a shows that with the optimization method, the maximum torque point is located at the 75-degree point. This distance is designed to be 15 degrees. Figure 8b illustrates the stator and rotor pole shapes from the optimization.
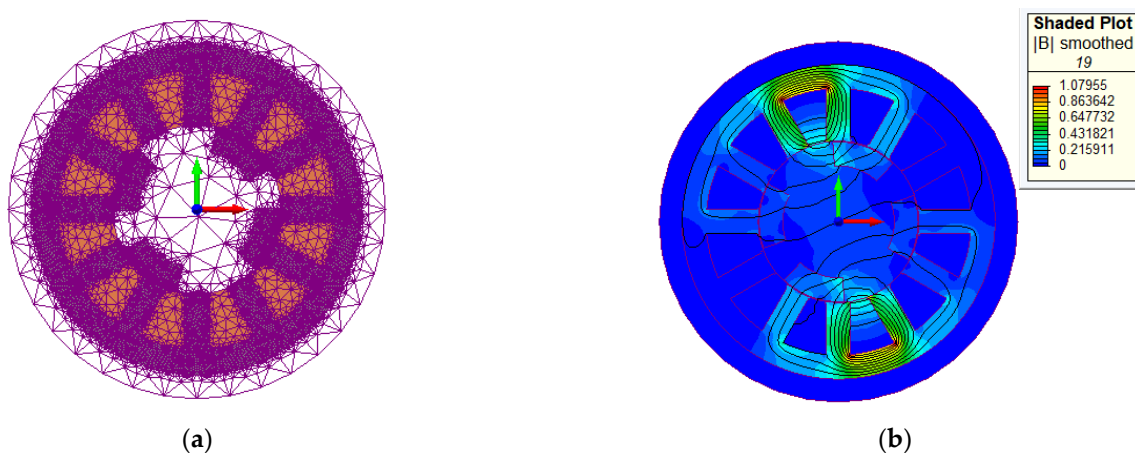

(**a**)

(**b**)

Figure 7. FEM simulation results of the proposed SRM: (**a**) the mesh distribution; (**b**) the magnitude of the magnetic flux density.

Table 2 lists the details of the optimization method. The objective is to minimize the distance between the maximum torque point and the 75-degree position. When the maximum torque point is fixed to the 75-degree position, the distance between the maximum torque point and the zero-torque point will be 15 degrees. The torque waveforms of the next phase are shifted by 15 degrees. As a result, the maximum torque point of the present phase will be in line with the zero-torque point of the next phase. Therefore, the torque ripple of the proposed SRM is reduced as illustrated in Figure 4. The degree-of-freedom is the width of the stator poles, and the constraint is to keep the slot area constant for the windings. The optimization algorithm used for this problem is the golden section search and parabolic interpolation algorithm [26,27].
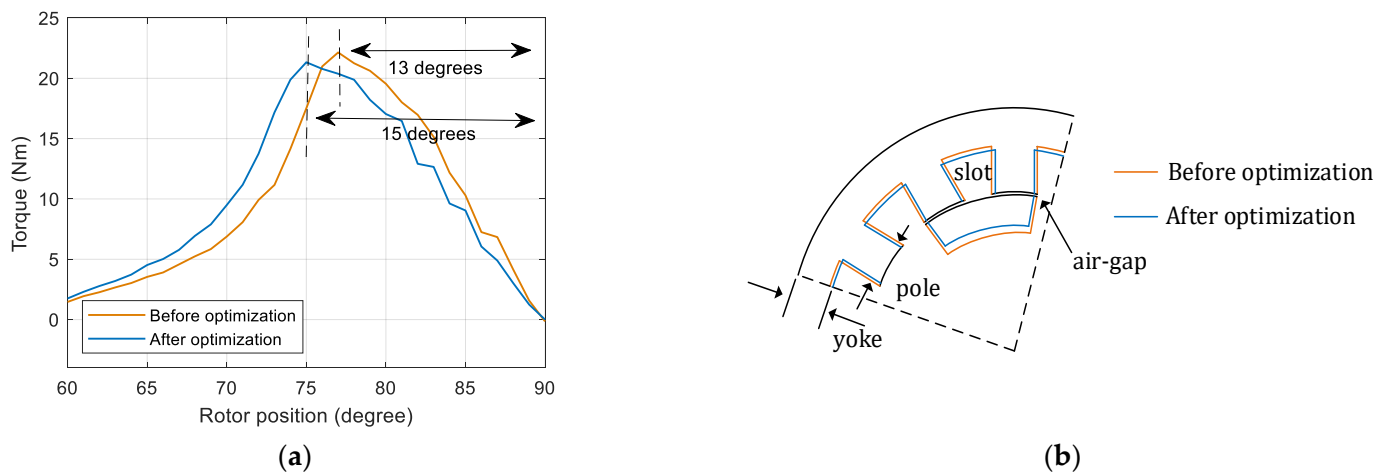
Figure 8. Optimization of the proposed SRM: (**a**) the optimization results of the torque; (**b**) the optimization result of the pole dimensions.

Table 2. The details of the optimization methods.

Objective	Minimization of the distance between the maximum torque point and the 75-degree position in Figure 8a
Variable	Width of the pole in Figure 8b
Constraint	The slot area is constant in Figure 8b
Optimization algorithm	Golden section search and parabolic interpolation algorithms

The optimization variable is the width of the stator poles in Figure 8b. Both the thickness of the stator yoke and the thickness of the rotor segments are equal to the thickness of the stator poles as shown in Figure 8b. The arc angle of the rotor segments is equal to the arc angle across two stator poles. The thickness of the stator yoke, the thickness of the rotor segments, and the arc angle of the rotor segments can be calculated from the width of stator poles, which is the optimization variable.

The values from the optimization results are listed in Table 3. As the optimization is performed and results obtained, the stator pole width is changed from 5 mm to 5.7 mm, the rotor pole arc is changed from 21.9 degrees to 22.9 degrees, and the rotor inner diameter is changed from 63.5 mm to 60.7 mm.

**Table 3.** SRM parameters before and after the optimization.

Parameter	Before Optimization	After Optimization
Stator pole width (mm)	5	5.7
Rotor pole arc (degree)	21.9	22.9
Rotor inner diameter (mm)	63.5	60.7

Figure 9 demonstrates the static profiles of the proposed SRM from the FEM simulation. Figure 9a shows that the middle points of the torque profiles are misaligned 15 degrees. Figure 9b presents that the middle points of the flux linkage profiles are misaligned by 15 degrees.

The torque can be expressed as:

$$T_e = \partial W_{em}(\theta, i)/\partial \theta = 1/2 \times i^2 \times dL/d\theta \tag{2}$$

where $W_{em}(\theta, i)$ is the magnetic co-energy, i is the current, θ is the rotor position, and T_e is the torque [28]. All units are according to S.I. units.

(**a**)

(**b**)
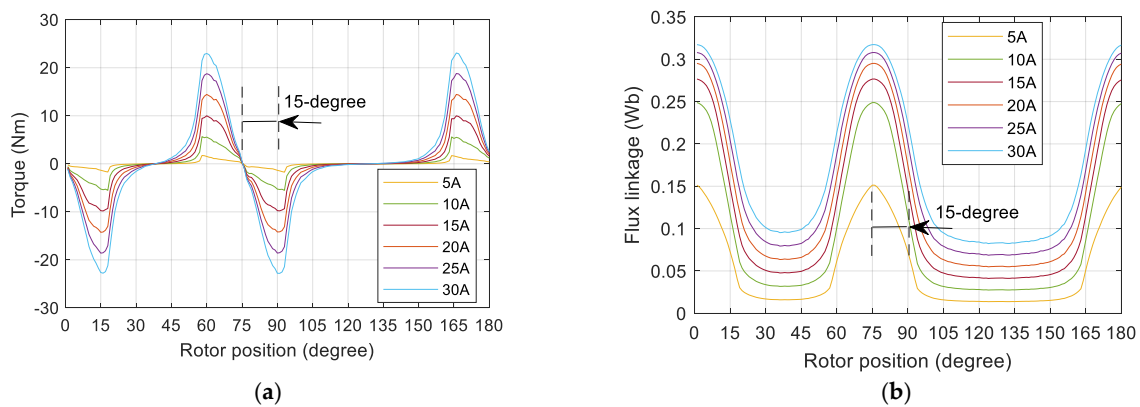
Figure 9. FEM simulation static torque and flux linkage profiles of the proposed SRM: (**a**) the static torque profiles; (**b**) the static flux linkage profiles.

Figure 10 presents the static performance from the FEM simulation of the proposed SRM. The FEM simulation is performed with the maximum current 35 A. The dashed line in Figure 10 shows the sum of the positive torques of each phase. It explains the method of the proposed SRM to reduce the torque ripple. Once the phases work in the sequence displayed in Figure 4, the output torque ripple will be reduced. Figure 11 displays the FEM simulation results of the conventional SRM with 35 A current. The average value of the static torque for the proposed SRM and the conventional SRM are 23.9 Nm and 6.6 Nm, respectively, as listed in Table 1. The difference is from the inductance difference of the two SRMs.
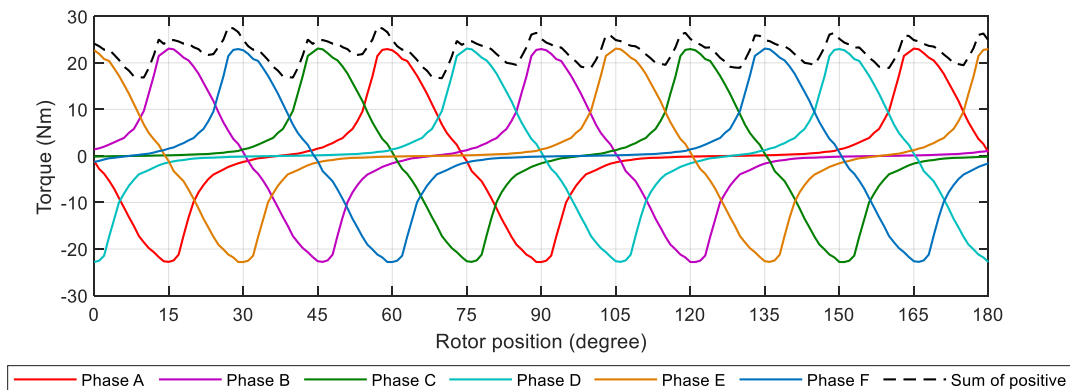
Figure 10. Static characteristics of the proposed SRM from FEM simulation results.
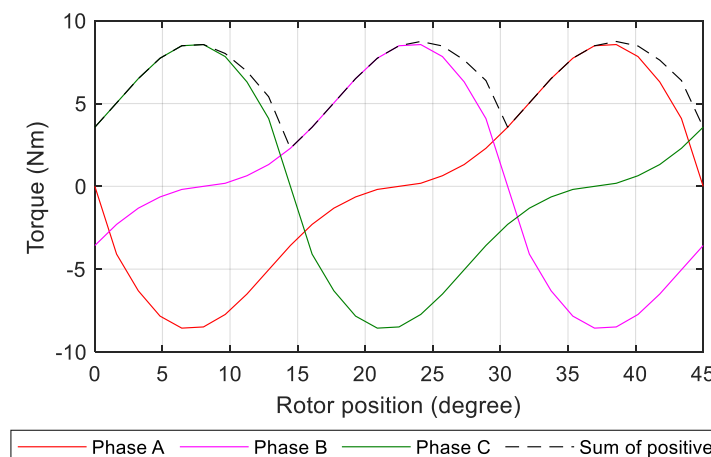
Figure 11. Static characteristics of the conventional SRM from FEM simulation results.

4. Cooling System Design

A water liquid cooling system with an aluminum machine cooling jacket is designed for the proposed SRM. It is used to prevent the SRM from overheating. The FEM method is used to analyze the cooling system. Figure 12 shows the schematic of the liquid cooling system. Figure 13a shows the CAD model of the liquid cooling jacket. Figure 13b shows the mesh distribution of the liquid cooling jacket and the SRM. The cooling jacket is directly connected to the stator yoke. The liquid cooling channel is made directly inside the jacket. Table 4 lists the parameters for the thermal analysis. When the phase current is 20 A, the copper losses are 528 W, and the maximum temperature reaches 29.9 °C. The temperature is in a safe range.
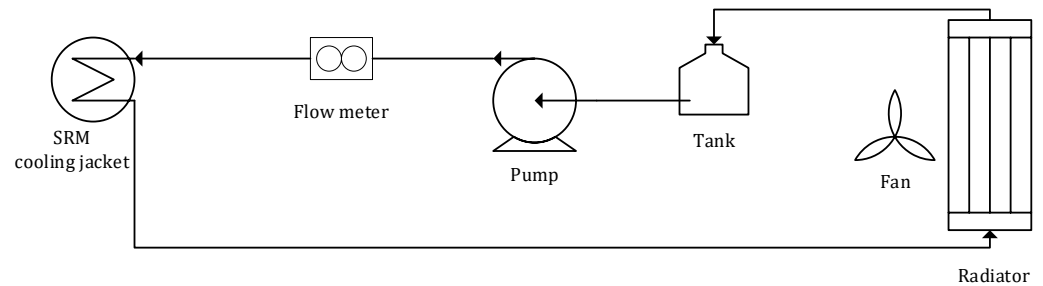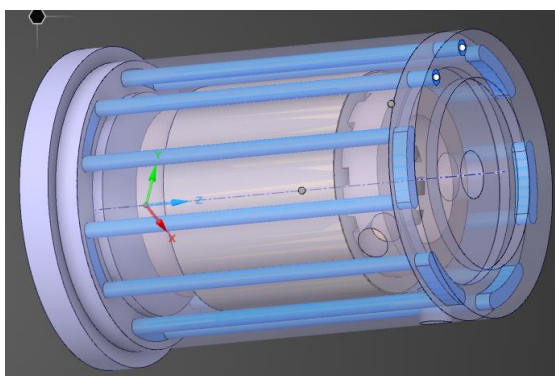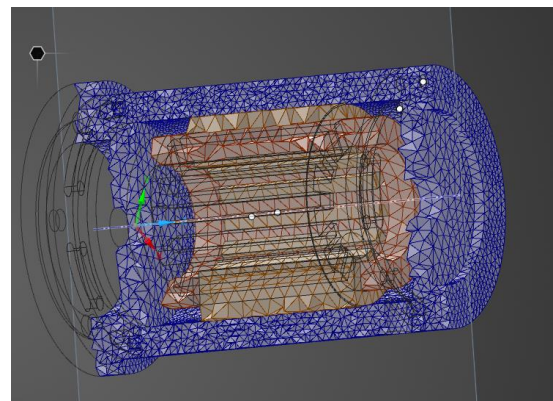

Figure 12. SRM cooling setup schematic.

(**a**)   (**b**)

Figure 13. Cooling jacket and the FEM analysis: (**a**) the CAD model of the cooling jacket and SRM; (**b**) the mesh distribution for the FEM simulation.

Figure 14 shows the FEM simulation results of the cooling system for the proposed SRM. It illustrates that the highest temperature areas are at the two end-windings zones.

Figure 15a presents the setup of the cooling system. Figure 15b illustrates the measured thermal results. From a hole for the cable terminal on the water jacket, the temperature of the stator can be observed. It is 26.4 °C as shown in Figure 15b.

Table 4. The loss parameters for the thermal analysis.

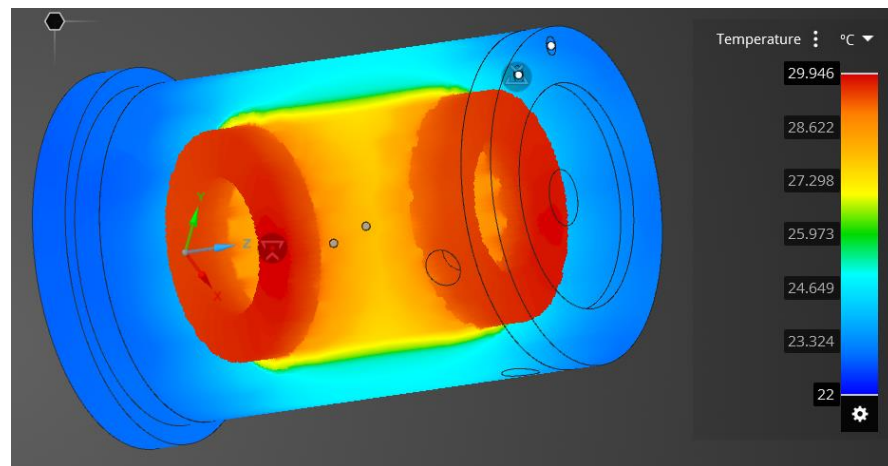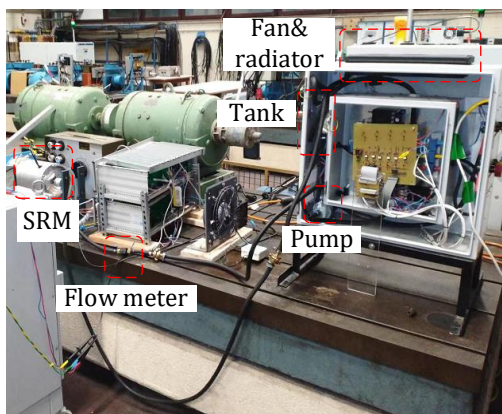| Phase Current (A)	Copper Losses (W)	Maximum Temperature (°C)
20	528	29.946

Figure 14. The FEM thermal simulation of the liquid cooling jacket.


(**a**)

(**b**)

Figure 15. The test of the cooling system: (**a**) the setup of the cooling system; (**b**) the measured thermal result.

5. Simulation and Analysis

The dynamic simulations are performed to validate the proposed SRM. MATLAB/ Simscape™ is used to simulate the SRM systems.

Figure 16 shows the drive and control system for the conventional SRM and the proposed SRM. SiC MOSFETs are used to create the driver as shown in Figure 16a. A dual-loop control system is used in the simulation and experiment. The current controller in Figure 16b is the hysteresis current controller. The speed controller is a PID controller.
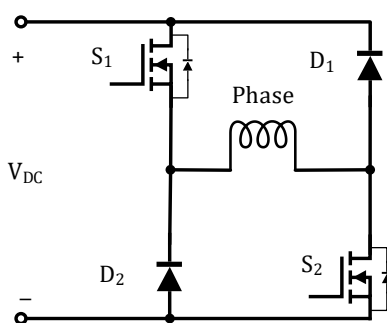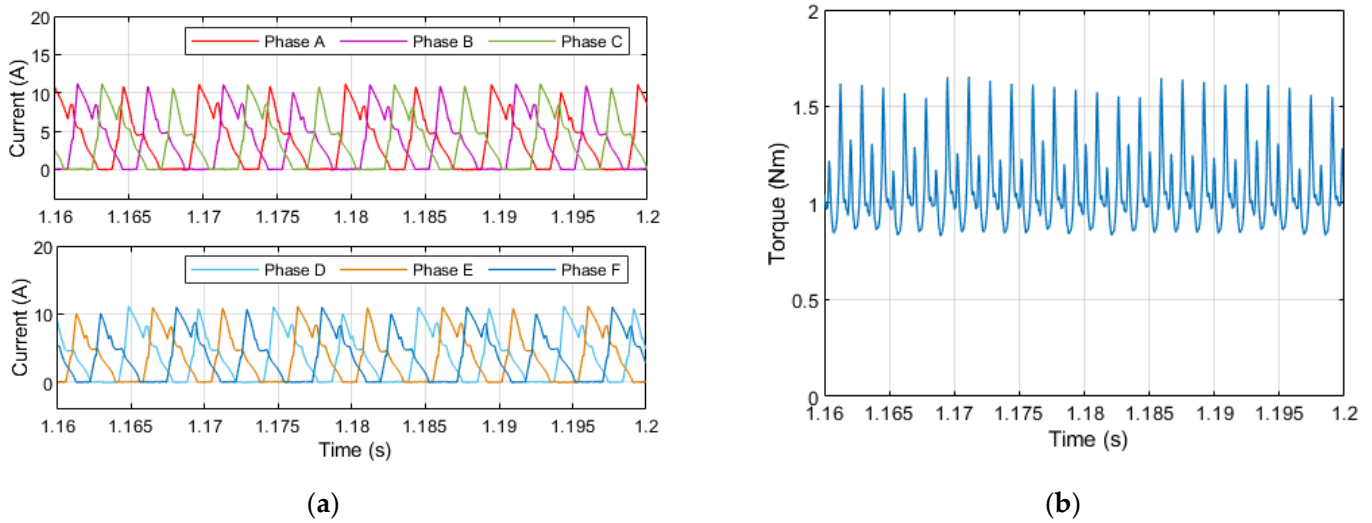

(**a**)
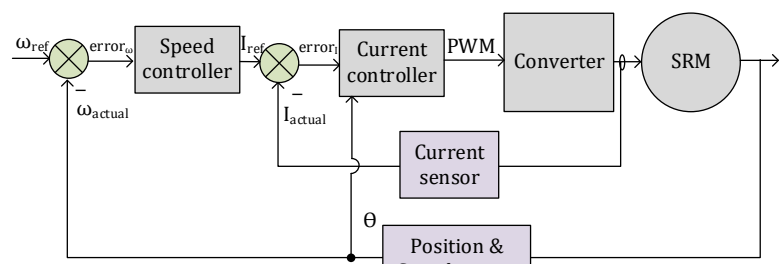
(**b**)

Figure 16. SiC driver and the control system: (**a**) SiC converter for each phase; (**b**) dual-loop control system diagram.

Figure 17 illustrates the simulated current waveforms and the torque waveform.

(**a**)

(**b**)

Figure 17. MATLAB/Simulink simulation results at 3000 rpm: (**a**) current waveforms. (**top**) Phase A, B and C, (**bottom**) Phase D, E and F; (**b**) torque waveform.

6. Prototype and Experimental Results

To verify the simulation results, a prototype of the proposed SRM is manufactured. A SiC MOSFET driver with a digital signal processor (DSP) controller is used to build the SRM drive system. A DC motor is used as the load machine. The field winding of the DC machine is connected to a DC voltage supply.

Figure 18 presents the prototype and setup of the proposed SRM. The torque sensor is used to measure the static and dynamic torque of the SRM.

Figure 19 illustrates the FEM results and measured static torque and the measured flux linkage for the proposed SRM. The measured results reach a good agreement with the FEM simulation results. The flux calculation is based on the measured torque.
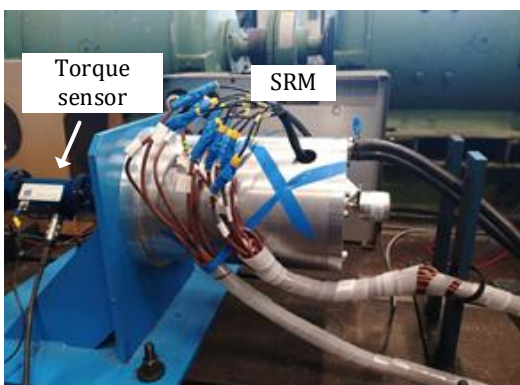

(**a**)
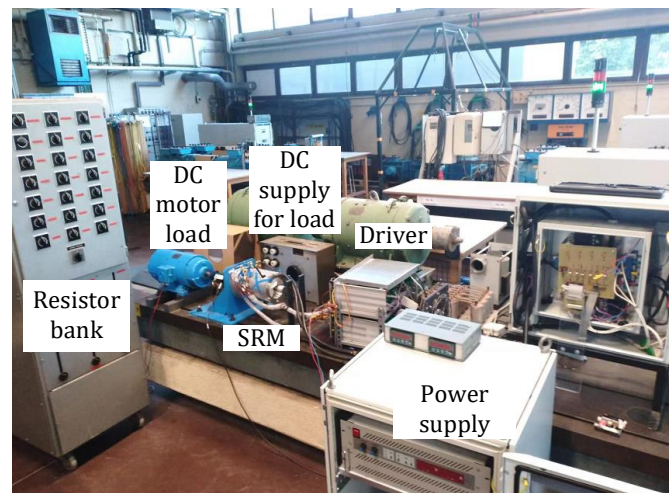
(**b**)

Figure 18. Prototype and setup of the proposed SRM: (**a**) the prototype of the proposed SRM; (**b**) the setup of the SRM system for the experiment.

The following equations present the relation between flux and torque [29].

$$W_{em}(\theta_0, i_0) = \int T(\theta, i_0)d\theta + L_0 \times i_0^2/2 \qquad (3)$$

$$\psi(\theta_0, i_0) = \partial W_{em}(\theta_0, i_0)/\partial i \tag{4}$$

where $T(\theta, i_0)$ is the torque, L_0 is the unaligned inductance of the SRM, which is measured to be 5.3 mH, i_0 is the phase current, $W_{em}(\theta_0, i_0)$ is the magnetic co-energy, and $\psi(\theta_0, i_0)$ is the flux linkage.
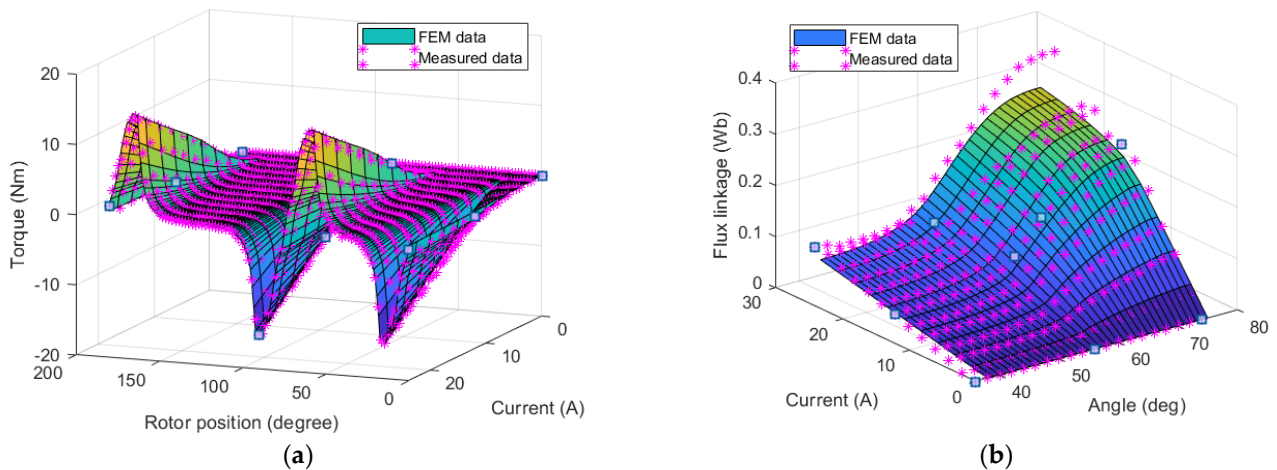

Figure 19. The FEM results and measured static data of the proposed SRM: (**a**) the torque; (**b**) the flux linkage.

Figure 20 presents the torque-speed specification for the 80 kW full-scale SRM and the 2 kW small-scale proposed SRM. For both SRMs, the rated speeds are 3000 rpm, and the maximum speeds are 6000 rpm. For the full-scale SRM, the rated torque is 254 Nm. The rated torque is 6.5 Nm for the small-scale SRM. In Figure 20, the tested points for this paper are marked.
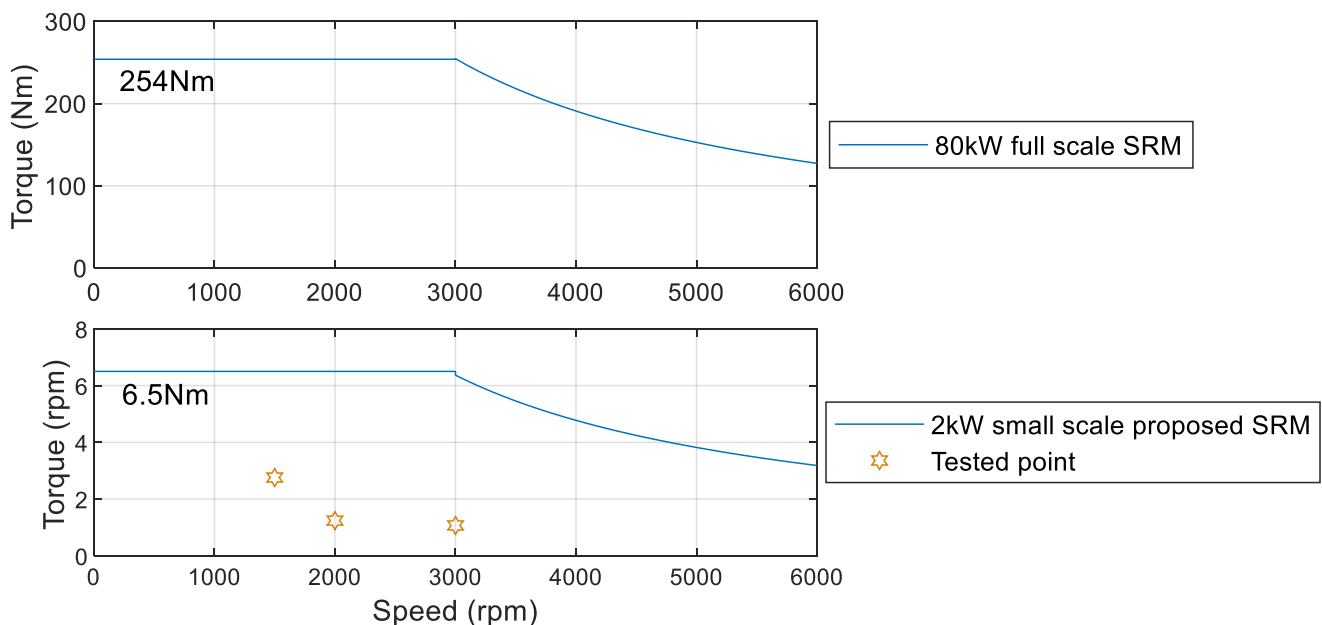

Figure 20. Torque speed specification for the full-scale SRM and the small-scale proposed SRM.

Figure 21a shows the proposed SRM experimental results of the current waveforms for phase A, B and C at a speed of 1500 rpm with load. Figure 21b shows the proposed SRM experimental current waveforms for phases D, E and F at 1500 rpm with load.
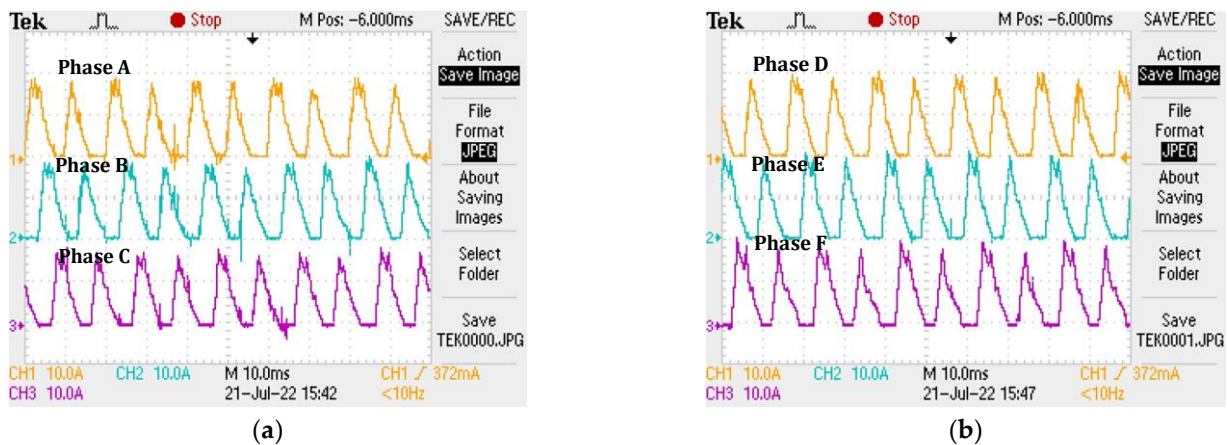
Figure 21. The proposed SRM experiment results of the phase current waveforms at 1500 rpm with load: (**a**) phase A, B and C current; (**b**) phase D, E and F current.

Figure 22 presents the reference SRM experiment results of the current waveforms at the speed of 1500 rpm with load. The current waveforms are used to reconstruct the accurate torque waveforms.
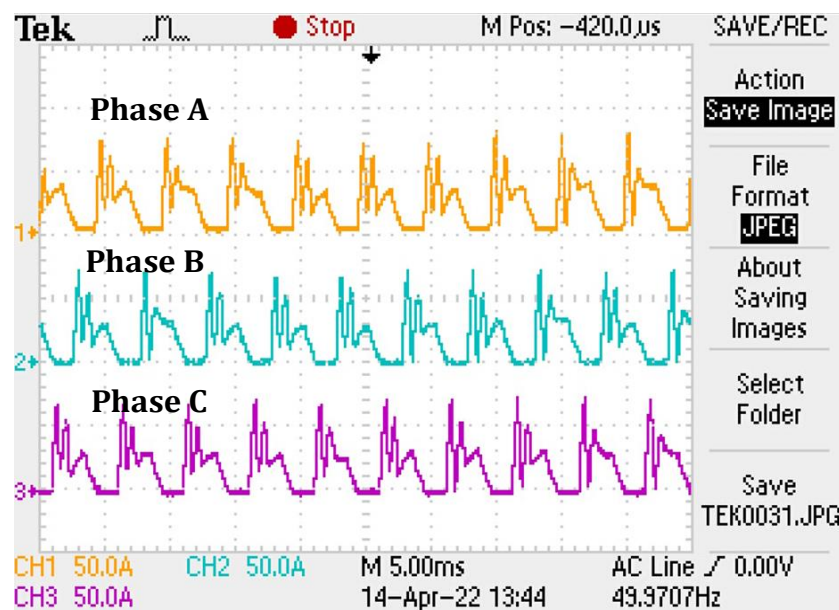

Figure 22. The reference SRM experiment results of the phase current waveforms at 1500 rpm with load.

The (3) expresses the definition of torque ripple:

$$T_r = (T_{max} - T_{min})/T_{avg} \tag{5}$$

where T_r is the torque ripple, T_{max} is the maximum torque, T_{min} is the minimum torque, and T_{avg} is the average torque.

Figure 23a shows the experimental result of the torque waveforms measured from the sensor on the shaft. It illustrates that the proposed SRM reduces the torque ripple by 45% at 1500 rpm compared to the conventional SRM. Figure 23b displays the torque ripple comparison from the sensor on the shaft for different speed values. It shows that the proposed SRM obtains lower torque ripple measured from the sensor on the shaft at different speeds compared to the conventional SRM.

(**a**)

(**b**)
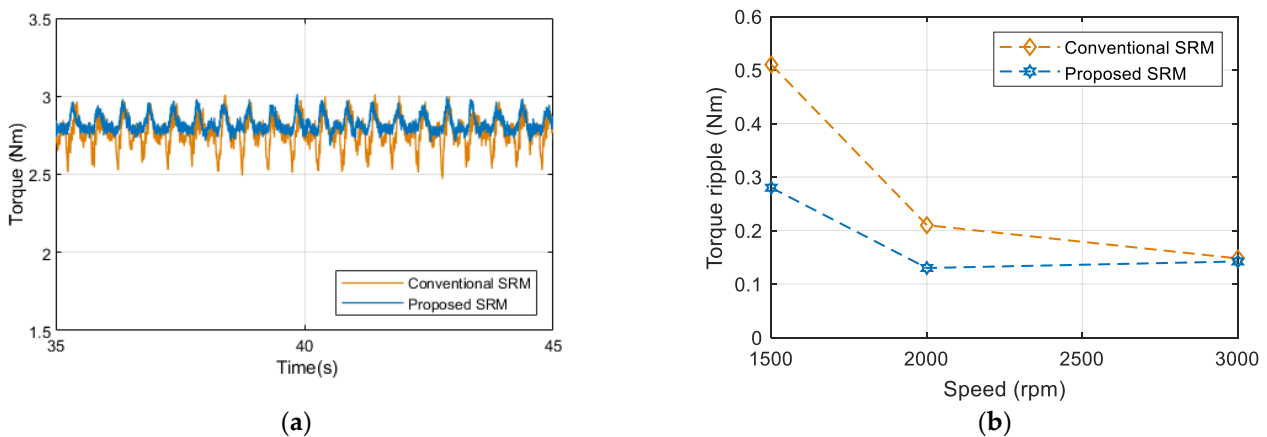
Figure 23. The experimental results from the sensor on the shaft: (**a**) torque waveforms at 1500 rpm; (**b**) torque ripple comparison at different speeds.

However, the torque waveforms measured from the sensor on the shaft are smoothed by the rotor. It should be reconstructed with the experiment current waveforms [30].

A simulink simulation is used to reconstruct the torque waveforms with the current waveforms from Figures 21 and 22. Figure 24 presents the reconstruction results with the 1500 rpm speed and 2.76 Nm torque load. Figure 24a displays the torque waveform and phase A current waveform for the proposed SRM. Figure 24b shows the torque waveform comparison. The torque ripple of the proposed SRM is reduced by 14.86%, compared to the reference SRM. Figure 24c displays the torque and phase A current waveforms for the reference SRM.

(**a**)

(**b**)

(**c**)
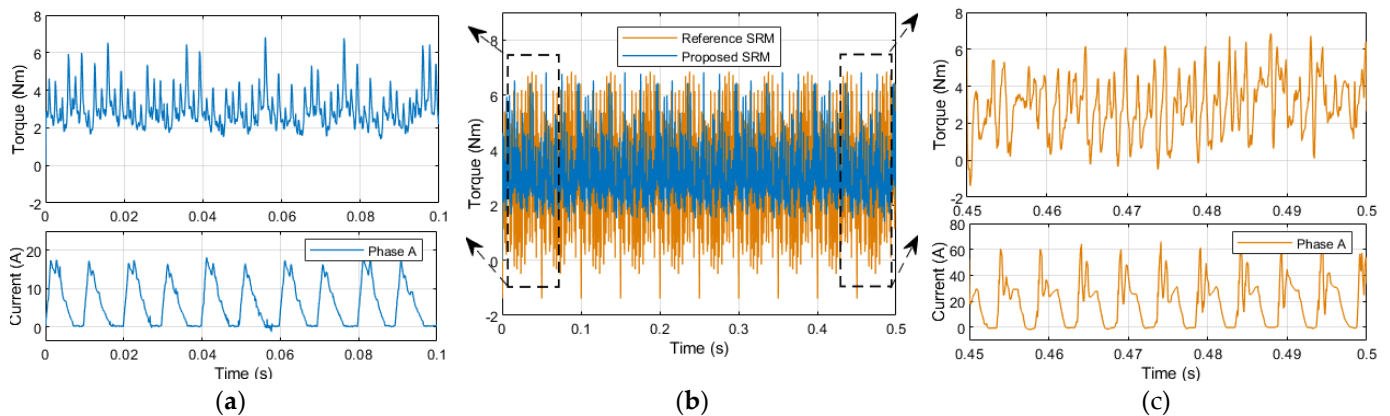
Figure 24. Torque reconstruction based on experiment results with 1500 rpm: (**a**) torque and current for the proposed SRM; (**b**) torque waveforms comparison; (**c**) torque and current for the reference conventional SRM.

Moreover, the mechanical size of the proposed SRM is the same as the conventional SRM as shown in Table 1.The rated power and torque of the proposed SRM are designed to be the same as the conventional SRM, which are 2 kW and 6.5 Nm, respectively.

7. Conclusions and Future Work

A six-phase SRM with a segmental rotor with a 15-degree misalignment is proposed in this paper for EV applications. With this misalignment, the proposed SRM torque ripple is reduced. At 1500 rpm, the torque ripple is reduced by 54.9%, compared to the conventional SRM. The FEM simulation is used to analyze and design the dimension of the proposed SRM, and an optimization method is used to determine the pole shapes of the stator and rotor, resulting in the 15-degree misalignment. A liquid cooling system is designed and analyzed using FEM software, which is subsequently tested with experiments. The dynamic

simulation of the SRM system is performed using a drive system with SiC MOSFETs. A dual-loop control system is built with a DSP. The prototype of the proposed SRM was manufactured and built, and experiments were performed to validate the torque ripple improvement of the proposed SRM. The experiment results show that the torque ripple of the proposed SRM is reduced for different speed ranges compared to the conventional SRM.

In the future, an advanced high-quality current controller will be further designed to generate smooth current waveforms. As a result, the torque ripple of the SRM will be further reduced. In addition, the electromagnetic interference (EMI) problem will also be limited. Furthermore, the efficiency and converter cost of the proposed SRMs compared to the interior permanent magnet machine should be analyzed comprehensively in future work. Finally, the copper length of the proposed SRM is long. It may increase copper losses and decrease SRM efficiency. It should be analyzed and updated in the future.

References

1. Kang, Z.; Hu, Y.; Sun, D. Multi-mode Drive Control System of Switched Reluctance Motor Based on a Novel N + 2 Power Converter. In Proceedings of the 2021 IEEE 4th Student Conference on Electric Machines and Systems (SCEMS), Huzhou, China, 1–3 December 2021.
2. Lan, Y.; Benomar, Y.; Deepak, K.; Aksoz, A.; Baghdadi, M.E.; Bostanci, E.; Hegazy, O. Switched Reluctance Motors and Drive Systems for Electric Vehicle Powertrains: State of the Art Analysis and Future Trends. *Energies* **2021**, *14*, 2079. [CrossRef]
3. Widmer, J.D.; Mecrow, B.C. Optimized Segmental Rotor Switched Reluctance Machines With a Greater Number of Rotor Segments Than Stator Slots. *IEEE Trans. Ind. Appl.* **2013**, *49*, 1491–1498. [CrossRef]
4. Widmer, J.D.; Martin, R.; Mecrow, B.C. Optimisation of an 80kW Segmental Rotor Switched Reluctance Machine for automotive traction. In Proceedings of the 2013 International Electric Machines & Drives Conference, Chicago, IL, USA, 12–15 May 2013.
5. Lan, Y.; Peng, W.; Aksoz, A.; Benomar, Y.; Van den Bossche, P.; El Baghdadi, M.; Hegazy, O. Design and Modelling of 12/4 Fully-Pitched Segmental Switched Reluctance Motors. In Proceedings of the 2020 Fifteenth International Conference on Ecological Vehicles and Renewable Energies (EVER), Monte-Carlo, Monaco, 10–12 September 2020.
6. Siadatan, A.; Najmi, V.; Asgar, M.; Afjei, E. A new 6/4 two layers switched reluctance motor: Concept, simulation and analysis. In Proceedings of the International Aegean Conference on Electrical Machines and Power Electronics and Electromotion, Joint Conference, Istanbul, Turkey, 8–10 September 2011.
7. Daldaban, F.; Ustkoyuncu, N. Multi-layer switched reluctance motor to reduce torque ripple. *Energy Convers. Manag.* **2008**, *49*, 974–979. [CrossRef]
8. Afjei, E.; Torkaman, H.; Mazloomnezhad, B. A new double layer per phase configuration for switched reluctance motor. In Proceedings of the 2010 IEEE International Conference on Power and Energy, Kuala Lumpur, Malaysia, 29 November–1 December 2010.
9. Siadatan, A.; Najmi, V.; Afjei, E. A novel 4/4 Multilayer Switched Reluctance Motor with 4 magnetically independent layers. In Proceedings of the International Aegean Conference on Electrical Machines and Power Electronics and Electromotion, Joint Conference, Istanbul, Turkey, 8–10 September 2011.
10. Vahedi, P.; Ganji, B.; Afjei, E. Multi-layer switched reluctance motors: Performance prediction and torque ripple reduction. *Int. Trans. Electr. Energy Syst.* **2020**, *30*, e12215. [CrossRef]
11. Higuchi, T.; Ueda, T.; Abe, T. Torque ripple reduction control of a novel segment type SRM with 2-steps slide rotor. In Proceedings of the The 2010 International Power Electronics Conference—ECCE ASIA, Sapporo, Japan, 21–24 June 2010.
12. Khor, M.T.; Sotudeh, R. A 3-phase 12/10 asymmetrical switched reluctance motor. In Proceedings of the 2005 European Conference on Power Electronics and Applications, Dresden, Germany, 11–14 September 2005.

13. Bogusz, P.; Korkosz, M.; Proko, J. Performance analysis of Switched Reluctance Motor with asymmetric stator. In Proceedings of the 2011 IEEE International Symposium on Industrial Electronics, Gdansk, Poland, 27–30 June 2011.

14. Bogusz, P.; Korkosz, M.; Powrózek, A.; Prokop, J. A two-phase switched reluctance motor with asymmetrical rotor for a high-speed drive. In Proceedings of the 2015 International Conference on Electrical Drives and Power Electronics (EDPE), Tatranska Lomnica, Slovakia, 21–23 September 2015.

15. Bogusz, P.; Korkosz, M.; Prokop, J. Control method of high-speed switched reluctance motor with an asymmetric rotor magnetic circuit. *Arch. Electr. Eng.* **2016**, *65*, 685–701. [CrossRef]

16. Torres, J.; Moreno-Torres, P.; Navarro, G.; Blanco, M.; Nájera, J.; Santos-Herran, M.; Lafoz, M. Asymmetrical Rotor Skewing Optimization in Switched Reluctance Machines Using Differential Evolutionary Algorithm. *Energies* **2021**, *14*, 3194. [CrossRef]

17. Xu, Z.; Yu, Q.; Zhang, F. Design and Analysis of Asymmetric Rotor Pole Type Bearingless Switched Reluctance Motor. *CES Trans. Electr. Mach. Syst.* **2022**, *6*, 3–10. [CrossRef]

18. Arbab, N.; Wang, W.; Lin, C.; Hearron, J.; Fahimi, B. Thermal Modeling and Analysis of a Double-Stator Switched Reluctance Motor. *IEEE Trans. Energy Convers.* **2015**, *30*, 1209–1217. [CrossRef]

19. Fairall, E.; Rheberhegen, C.; Rowan, E.; Lo, J.; Bilgin, B.; Emadi, A. Maximizing thermal effectiveness and minimizing parasitic loss in a liquid cooled switched reluctance machine. In Proceedings of the 2016 IEEE Transportation Electrification Conference and Expo (ITEC), Dearborn, MI, USA, 27–29 June 2016.

20. Márquez-Fernández, F.J.; Potgieter, J.H.J.; Fraser, A.G.; McCulloch, M.D. Experimental Validation of a Thermal Model for High-Speed Switched Reluctance Machines for Traction Applications. *IEEE Trans. Ind. Appl.* **2018**, *54*, 3235–3244. [CrossRef]

21. Ru, L. Comparison of Vibration Between an Evaporative Cooling Switched Reluctance Motor and a Conventional Switched Reluctance Motor. In Proceedings of the 2018 21st International Conference on Electrical Machines and Systems (ICEMS), Jeju, Korea, 7–10 October 2018.

22. Nonneman, J.; Schlimpert, S.; T'Jollyn, I.; De Paepe, M. Modelling and Validation of a Switched Reluctance Motor Stator Tooth with Direct Coil Cooling. In Proceedings of the 2020 19th IEEE Intersociety Conference on Thermal and Thermomechanical Phenomena in Electronic Systems (ITherm), Orlando, FL, USA, 21–23 July 2020.

23. Schlimpert, S.; Mrak, B.; Siera, I.; Sprangers, R.; Nonneman, J.; De Paepe, M.; Vanhee, S. Experimental & Modelling Study of Advanced Direct Coil Cooling Methods in a Switched Reluctance Motor. In Proceedings of the 2020 IEEE Vehicle Power and Propulsion Conference (VPPC), Gijon, Spain, 18 November–16 December 2020.

24. Lukman, G.F.; Nguyen, X.S.; Ahn, J.W. Design of a Low Torque Ripple Three-Phase SRM for Automotive Shift-by-Wire Actuator. *Energies* **2020**, *13*, 2329. [CrossRef]

25. Ma, C.; Qu, L.; Tang, Z. Torque ripple reduction for mutually coupled switched reluctance motor by bipolar excitations. In Proceedings of the 2013 International Electric Machines & Drives Conference, Chicago, IL, USA, 12–15 May 2013.

26. Grund, F.; Forsythe, G.E.; Malcolm, M.A.; Moler, C.B. Computer Methods for Mathematical Computations. Englewood Cliffs, New Jersey 07632. Prentice Hall, Inc., 1977. XI, 259 S. *Z. Angew. Math. Und Mech.* **1979**, *59*, 141–142. [CrossRef]

27. Brent, R.P. *Algorithms for Minimization without Derivatives*; Prentice-Hall: Englewood Cliffs, NJ, USA, 1973.

28. Zhou, Y.; Jiang, J.; Hu, P.; Yuan, Y. A Novel Dual-Channel Bearingless Switched Reluctance Motor. *IEEE Access* **2021**, *9*, 122373–122384. [CrossRef]

29. Cailleux, H.; Mouchoux, J.C.; Multon, B.; Hoang, E.; Le Chenadec, J.Y. Comparison of Measurement Methods to Determine the Electromagnetic Characteristics of Switched Reluctance Motors. In Proceedings of the Electric Drive Design and Applications, Lausanne, Switzerland, 19–20 October 1994; pp. 639–644.

30. Lukman, G.F.; Ahn, J.-W. Torque Ripple Reduction of Switched Reluctance Motor with Non-Uniform Air-Gap and a Rotor Hole. *Machines* **2021**, *9*, 348. [CrossRef]